Protective potential of high-contrast mineral-bonded layers on reinforced concrete slabs subjected to uniform shock waves

Lena Leicht [a,*], Matteo Colombo [b], Paolo Martinelli [b], Cesare Signorini [c], Viktor Mechtcherine [c], Marco di Prisco [b], Silke Scheerer [a], Manfred Curbach [a], Birgit Beckmann [a]

[a] Technische Universität Dresden, Institute of Concrete Structures, 01062 Dresden, Germany
[b] Politecnico di Milano, Department of Civil and Environmental Engineering, Piazza L. da Vinci 32, 20133 Milan, Italy
[c] Technische Universität Dresden, Institute of Construction Materials, 01062 Dresden, Germany

ARTICLE INFO

ABSTRACT

This study compares the blast performance of reinforced concrete (RC) slabs with and without strengthening on the impact-facing side. The strengthening strategy employed the application of two thin layers of materials with a high mutual stiffness offset, i.e., high-contrast layers. The first is a low-strength, low-modulus damping layer made of infra-lightweight concrete, followed by a second layer of high-ductility fiber-reinforced concrete. The plain RC slabs under investigation vary in thickness of either 40 mm or 100 mm. The layered specimens consist of a 40 mm thick RC slab strengthened with a 40 mm damping layer and a 20 mm cover $SHLC^3$ layer. This configuration enables a comparison of its behavior with the unstrengthened specimen (a plain 40 mm thick RC slab) and a specimen with a similar eigenfrequency (the plain 100 mm thick RC slab). The employed shock tube subjects the specimens to two rapidly rising areal pressures: a low-pressure wave reaching approximately 0.4 MPa and a high-pressure wave peaking at around 1.2 MPa. The study assesses the specimens' response in terms of accelerations, velocities, and deformations. Additionally, it evaluates damage by analyzing crack patterns, Ultrasonic Pulse Velocity (UPV) measurements, and damping analysis. Overall, the layered specimens exhibited performance nearly equivalent to the 100 mm thick specimens, displaying similar deformations and velocities despite having lower mass and bending stiffness. The high-pressure shock wave hardly damaged the layered specimens, unlike the 40 mm thick slabs.

1. Introduction

Reinforced concrete (RC) is the most common structural material adopted not only for residential and commercial buildings but also for infrastructures like bridges, tunnels, and dams. These kinds of constructions can be regarded as high-level-of-consequence constructions in the case of an inauspicious accidental action like a blast. For this reason, on the one hand, the design of new construction needs to adopt proper strategies to guarantee the structure's safety in this condition. On the other hand, existing structures must also be retrofitted to minimize possible damage. A typical blast event generally incorporates the effect of both shock wave propagation and fragmentation. The first causes a fast varying pressure to be applied to the structure. In the latter case, fragments accelerated by the shock wave act like projectiles impacting the structural elements [1]. The brittleness of concrete can lead to severe spalling and scabbing damage [2,3]. As an example, KÜHN ET AL. [4] performed full-scale blast experiments on concrete slabs. The slabs were 1,500 mm by 1,500 mm wide and 300 mm thick, and

the TNT equivalent of the explosive was 1 kg. The distance between the charge and the tested unstrengthened RC slabs was 50 mm. The introduced pressure wave had a peak incident pressure of 56 MPa and a reflected pressure of 681 MPa, leading to extensive compression and shear damage on the blast-facing side. Moreover, the blast ejected a considerable amount of spalling mass at the bottom of the slab.

An effective retrofitting solution for the blast-facing side of the structure needs to be able to mitigate both these effects in order to fully protect the structure from extreme events. Strengthening layers are the most common solution for these kinds of interventions. SCHENKER ET AL. [5] showed the effectiveness of protective layers made of aluminum foam. They tested unstrengthened and strengthened RC slabs with a span of 3 m. The strengthening consisted of two types of aluminum foam covered with steel plates applied to the impact-facing side of the structure. The peak pressure was 0.65 MPa. The protection reduced both the slab's damage and the peak accelerations.

The literature also proposes the use of a cement-based layered solution as an effective method to mitigate the impact of blast actions.

---

* Corresponding author.
E-mail address: lena.leicht@tu-dresden.de (L. Leicht).

COLOMBO ET AL. [6] tested layered tunnel segments consisting of High-Performance Fiber-Reinforced Cementitious Composite (HPFRCC) and Steel Fiber-Reinforced Concrete (SFRC) supported by soil, designed as new, blast-resistant tunnel segments. The thicker three-layered structure, consisting of two cover layers of HPFRCC incorporating a core of SFRC, exhibited a higher bending stiffness than the two-layered structure and, thus, a lower soil deformation. After the experiment, the authors did not record any delamination of the three layers. In the case of the two-layered structure made of only an SFRC core and an HPFRCC rear side layer, slight delamination occurred due to the blast load applied.

RC panels strengthened with Strain-Hardening Cementitious Composite (SHCC) only on the blast-far or on the blast-near and -far side proved a higher blast resistance of such panels compared to unstrengthened counterparts [7]. The panels strengthened on both sides even outperformed the ones strengthened on the rear side in terms of reducing maximum and residual displacement.

Using different Carbon Fiber Reinforced Polymer (CFRP) strips applied to strengthen the rear side of RC beams also reduced the maximum deformations and the strains in the tensile reinforcement of the beams. However, the strengthening increased the compressive damage on the loaded top side of the beams [8].

HAJEK ET AL. [9] compared the behavior of a barrier on the blast-facing side made of foam pyramidal acoustic panels to that of truncated pyramids consisting of Ultra-High Performance Fiber-Reinforced Self-Compacting Concrete (UHPFRSCC). Although the soft material of the acoustic panels absorbed more energy and hence reduced the peak overpressure to a greater extent, its residual deformation can cause damage to the sheeting panel. The energy absorption due to plastic deformation of the UHPFRSCC panel was negligible. Nevertheless, both structures showed similar blast mitigation properties. Moreover, the UHPFRSCC panel's blast wave mitigation effect was very pronounced, and it offers the advantage of being fire-resistant, durable, and able to stop fragments.

In addition, the use of multi-layer protective solutions on the impact-facing side comprising materials with significant stiffness and strength offset, generally referred to in the literature as "high-contrast" [10], is often considered as a possible strategy for protection against localized impact loads. In these situations, the cover layer aims to distribute the impact load in order to activate larger parts of the damping layer, whose primary goal is to dissipate energy by plastic deformation or internal friction and reduce the impact force or to act elastically to favor an impactor rebound.

In the literature, some examples of naturally occurring layered solutions are available (e.g., crustacean exoskeletons [11], seashells [12, 13]). Fruit peels such as those of pomelos [14] also serve as an example of impact protection. The peel has a foam-like core that can be compressed up to 40 % when the fruit falls on the ground and hence protects the interior of the fruit. Such naturally inspired solutions were applied to the impact-facing side of RC structures and firstly tested under hard impact loading [15], i.e., at high impact velocity using a non-deformable impactor [2,16,17]. Such loading represents the flying debris that follows a blast event. LEICHT [15] has proved that a really effective strengthening option under these loading conditions was found to be made of a 40 mm thick Infra-Lightweight Concrete (ILC) damping layer covered by a Strain-Hardening Limestone Calcined Clay Cement (SHLC^3) cover layer. This combination was tested under drop tower impact loads at high impact velocities of up to 55 m/s with a solid steel impactor weighing 21.66 kg. This strengthening option halved the maximum impact forces inhibiting the damage to the RC structures. The force reduction, in this case, was due to the severe crushing and densification of the ILC damping layer, whose effect on the performance of the strengthening layer was more pronounced than that of the SHLC^3 cover layer [15].

Having demonstrated the effectiveness of the developed layered strengthening strategy for the impact-facing side comprising ILC and

SHLC^3 against localized, hard, and fast impacts, the current objective was to assess its performance under blast loading. Hence, this study focuses on evaluating the behavior of the developed impact strengthening under blast loading, precisely uniform shock-wave loading. Investigating both blast-induced phenomena is crucial for understanding the behavior of the strengthening layer under extreme loading conditions and for providing essential input data for potential upscaled simulations involving walls and columns that could benefit from these layers.

An experimental campaign was planned at the Politecnico di Milano, where a shock tube facility for testing small-scale structural elements is available. This equipment generates a shock wave whose reflection on the structural sample loads it with a rapidly varying pressure distribution [18,19]. The experimental campaign aims at assessing the performance of an RC slab blast-side strengthened with the ILC and SHLC^3 layer and presents a comparison with the behavior of thin, unstrengthened RC slabs (considered as the reference structure to be retrofitted) and that of RC slabs with an elevated thickness equaling that of the layered option. The experimental program involves two loading pressures. Generally, each combination of specimen type and loading pressure was repeated twice.

2. Experimental campaign

2.1. Specimen design and geometry

As previously described, the primary focus of this investigation was to evaluate the performance of a layered retrofitting solution under shock-wave loading. This solution employs cement-based materials, specifically Infra-Lightweight Concrete (ILC) and Strain Hardening Limestone Calcined Clay Composite (SHLC^3) applied to the blast-facing side.

The experimental program comprised three different types of circular concrete slabs with a diameter of 690 mm, as also shown in Fig. 1:

(a) 40 mm thick RC slabs of concrete class C35/45 (labeled as RC-40 hereafter),

(b) 100 mm thick RC slabs of concrete class C35/45 (labeled as RC-100 hereafter),

(c) layered slabs consisting of a 40 mm thick RC base slab of concrete class C35/45, strengthened with a 40 mm thick damping layer made of ILC and a 20 mm thick cover layer made of SHLC^3 (labeled as LAY hereafter).

In this study, the 40 mm thick RC slabs (RC-40) were intended as a benchmark to determine the improvement of the structural behavior due to the addition of the strengthening layer. In addition, 100 mm thick concrete slabs (RC-100) served as a further reference case scenario. In fact, while the layered structure works well under localized hard impact, adding more ordinary concrete to existing elements does not, as this method cannot reduce the impact force and hence cannot obviate spalling and scabbing damage under localized impact loading. Nevertheless, the higher bending stiffness and eigenfrequency may likely improve the bearing capacity under shock-wave loading to some extent. This sample can be regarded as a retrofitting solution in which the existing concrete structure is strengthened by just increasing the thickness of the structure by ensuring a perfect bond with the existing substrate. It is worth noting that this sample's thickness was defined to have a similar first natural frequency as the layered slabs.

Regarding the calculation of the first natural frequency, the assumption of a perfect bond between the layers enabled the estimation of the bending stiffness and eigenfrequency of the layered slabs with the composite modulus of elasticity and geometrical moment of inertia. To calculate the initial, linear-elastic equivalent composite modulus E_{eq} of the LAY specimens, the individual values of the bending stiffness EI of the respective layers (SHLC^3, ILC, C35/45, and reinforcement) were calculated compared to the global centroid of the entire composite
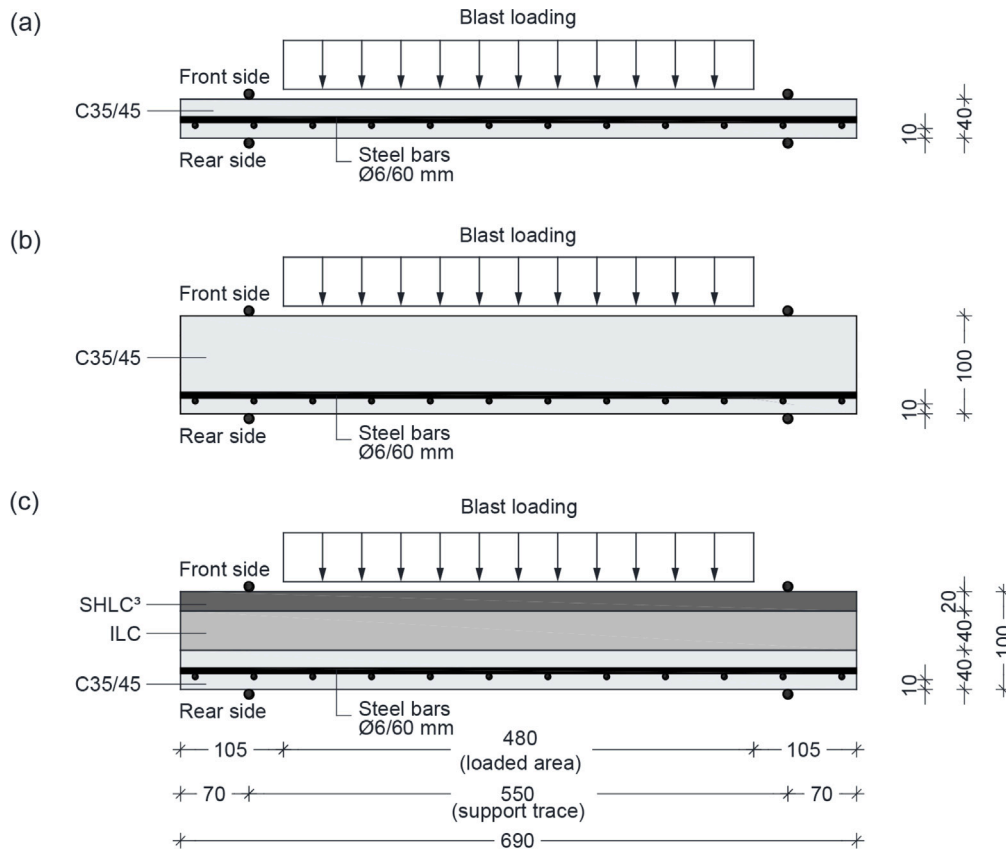
Fig. 1. Specimen dimensions: (a) 40 mm thick RC specimens (RC-40); (b) 100 mm thick RC specimens (RC-100); (c) 100 mm thick layered specimens (LAY) (dimensions in mm).

structure. Afterward, these values were summed up to a global value of EI. Dividing the global EI value by the moment of inertia of the entire slab yields the equivalent composite modulus (see Eq. (1)).

$$E_{eq} = \frac{EI_{SHLC^3} + EI_{ILC} + EI_{C35/45} + EI_{reinforcement}}{h_{slab}^3/12} \quad (1)$$

The first circular frequency (ω_1) was calculated based on Eq. (2) for simply supported, circular slabs [20]:

$$\omega_1 = 0.811 \cdot \sqrt{E \cdot h^3/(m \cdot D^2)} \quad (2)$$

where E is the modulus of elasticity, h is the thickness, m is the mass, and D is the slab diameter. In the case of the layered specimens, E represents the equivalent composite modulus ($E = E_{eq}$), considering a full specimen height of 100 mm.

Table 1 allows for a comparison of the calculated values of the different samples. The specimen type affects the bending stiffness most severely. The influence of the specimen type on its mass and eigenfrequency is smaller than that on the bending stiffness. The difference between the masses of the RC-100 and the layered specimens is more significant than the difference between the two first circular frequencies. Conversely, an opposite trend is observed between the RC-40 and the layered slab. The percentage values in Table 1 represent the absolute values of the respective properties compared to those of the LAY specimens.

2.2. Raw materials and specimen preparation

The base material of all tested slabs was a normal-strength concrete of the class C35/45 [21]. A mild steel (grade B500B) mesh including bars with a diameter of 6 mm and a grid size of 60 mm was designed as the internal reinforcement for the C35/45 layer. Table 2 displays the material properties of the C35/45 base slabs and the material

Table 1
Comparison of the structural behavior of the different slab variants.

	RC-40	RC-100	LAY
Mass (kg)	22.2	50.7	42.9
Bending stiffness (EI) (kNm)	182.8	2,692.2	2,199.2
First circular frequency (rad/s)	463.4	1,177.6	1,156.4
First frequency (Hz)	73.7	187.4	184.0
Mass (%)	52	118	100
Bending stiffness (EI) (%)	8	122	100
First circular frequency (%)	40	102	100
First frequency (%)	40	102	100

properties of the used cementitious strengthening layer materials. The ILC served as the damping layer and was covered by the stiff SHLC³ layer. Leicht [15] presents details of the mix compositions. The mean compressive strengths and moduli of elasticity were determined on four cylinders with a height of 300 mm and a diameter of 150 mm. Dog-bone-shaped specimens with a total length of 455 mm and a tapered length of 375 mm were tested to ascertain the tensile strength. Their cross-section in the gauge section was 50 mm×50 mm. The tests for the determination of the material parameters (see Table 2) were performed slightly after the shock tube experiments. The ages of the shock tube specimens are presented in Table 4.

Regarding the specimen preparation and curing, the RC-40 and RC-100 samples were stored at ambient temperature and humidity after casting. Consequently, the higher compressive strength and the higher modulus of elasticity obtained for the C35/45 layer of the RC-40 slabs are merely ascribed to their older age (see Table 2). In the case of the layered specimens, the casting also began with the C35/45 layer. Retardation paper was applied atop the base layer to ensure sufficient surface roughness after washing with water, exposing the aggregates and facilitating a strong bond with the subsequent ILC layer. Two weeks

Table 2
Material properties of the C35/45 base slabs and the strengthening layer materials. Mean represents the mean value and SD is the standard deviation of the individual values.

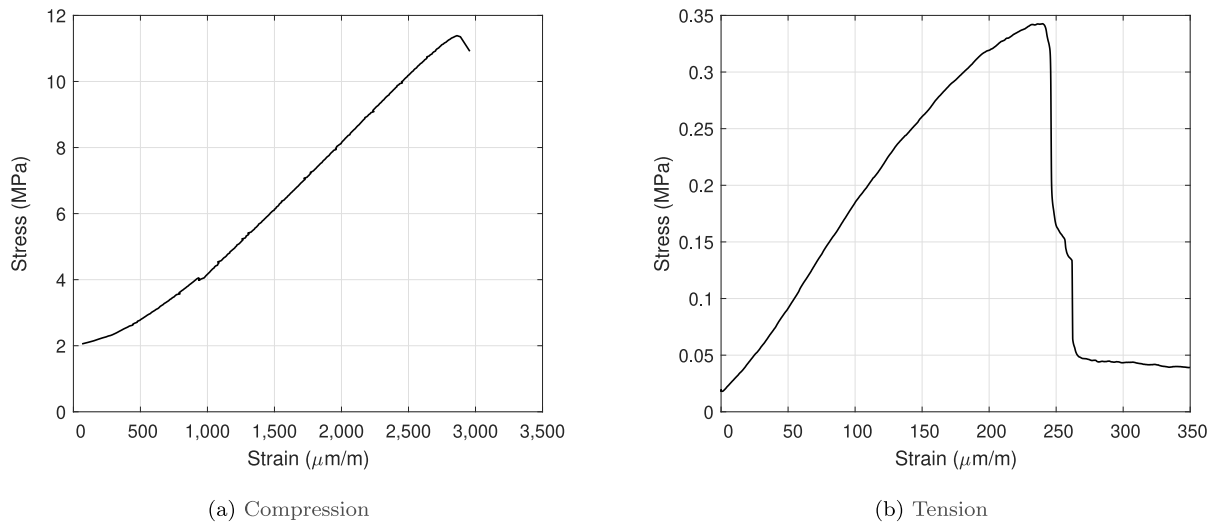|	Age	Compressive strength		Tensile strength		Density		Modulus of elasticity	
	(d)	(MPa)		(MPa)		(kg/m^3)		(MPa)	
		Mean	SD	Mean	SD	Mean	SD	Mean	SD
C35/45 (RC-40)	213	41.8	2.2	2.7	0.1	2,245	6	34,000	265
C35/45 (RC-100)	71	31.7	0.8	3.2	0.2	2,095	17	31,000	1,253
C35/45 (LAY)	141	50.3	0.5	4.1	0.8	2,268	5	34,233	1,332
ILC	127	11.8	0.5	0.3	0.0	1,163	17	5,433	551
SHLC^3	106	88.1	2.4	3.6	0.3	1,984	21	25,600	361

(a) Compression

(b) Tension

Fig. 2. Representative quasi-static stress–strain curves of ILC.

after casting the base slab, the ILC layer was added. The layered and all corresponding reference specimens were water-stored one day after the second casting. Retardation paper was not required on the top of the ILC layer as the aggregates on the top side of this material were already exposed, ensuring a stable bond to the SHLC^3 layer. The SHLC^3 was applied three weeks after the second casting. After one day, water-storing of the layered and all corresponding reference specimens was arranged. The water storage of the layered specimens and the corresponding material characterization samples was most likely the reason for the superior material properties of the C35/45 layer observed (see Table 2). Water storage was organized to ensure that the different shrinkage did not damage the materials or the bond between them.

A better insight into the material behavior of the strengthening layer materials is given with their stress–strain curves. The damping layer is made of ILC, composed of a cement matrix with expanded clay aggregates. It behaves brittle under both compressive and tensile loading and possesses a low strength and modulus under both loading conditions (see Fig. 2). This complies with the desired behavior for the soft damping layer.

The composition of the SHLC^3, which constitutes the stiff cover layer in the layered configuration, is provided in detail by SIGNORINI ET AL. [22]. The representative stress–strain behavior is given in Fig. 3. The compressive strength at 28-day curing is 83.2 MPa ($\pm$5.2 %), whereas the tensile strength is 4.3 MPa ($\pm$4.5 %). The high strength is desired for the strong cover layer material.

2.3. Shock tube facility and loading conditions

The experimental campaign was performed at the Impact and Explosion Lab of Politecnico di Milano by the use of a double diaphragm shock tube equipment. A detailed description of the instrumentation is

available in COLOMBO ET AL. [18,23]. The whole shock tube can move on a linear guide system and consists of three main sections, i.e., a driver, a diaphragm, and a driven chamber (Fig. 4). Two scored S235R steel diaphragms having a circular shape, a diameter of 697 mm and a thickness of 2 mm, i.e., metallic discs, separate the diaphragm chamber from the other two. A detailed description of the steel diaphragms used in the experiments is presented in ANDREOTTI ET AL. [19]. Before the initiation of the experiment, a vacuum pump creates a vacuum in the driver and diaphragm chambers. Then, helium fills the driver chamber to half of the target test pressure. Afterward, the diaphragm chamber is filled to the requested pressure, and then the pressure in the driver chamber reaches the target pressure for the experiment. Upon opening the valves of the diaphragm chamber, the pressure in the driver chamber overcomes the bearing capacity of the diaphragm toward the diaphragm chamber, which ruptures. Right afterward, the pressure also destroys the second diaphragm toward the driven chamber. Then, the pressure wave travels through the shock tube, reaching the specimen as a planar pressure. The pressure sensors measure the applied pressure before reaching the specimen surface.

Two different pressure histories were selected for the tests, resulting from setting two different levels of pressure within the driver and diaphragm chambers. The first set of experiments, referred to as low-pressure (LP) experiments, utilized absolute pressures of 5.4 bar and 3.2 bar in the driver and diaphragm chambers, respectively. The second set, referred to as high-pressure (HP) experiments, employed an absolute pressure of 15 bar in the driver chamber and 8 bar in the diaphragm chamber. In all experiments, the driven chamber contained air at ambient conditions, while the driver and diaphragm chambers were pressurized with helium after being evacuated to approximately −800 mbar relative to ambient pressure. A summary of the initial conditions in the shock tube chambers during both sets of experiments is presented in Table 3.
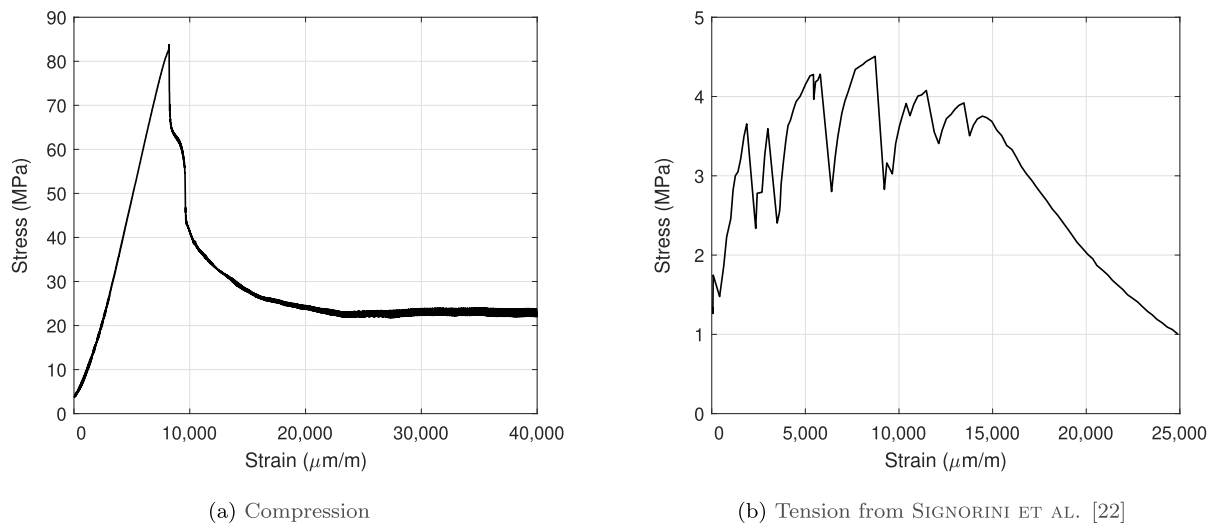
(a) Compression

(b) Tension from SIGNORINI ET AL. [22]

Fig. 3. Representative quasi-static stress–strain curves of SHLC^3.
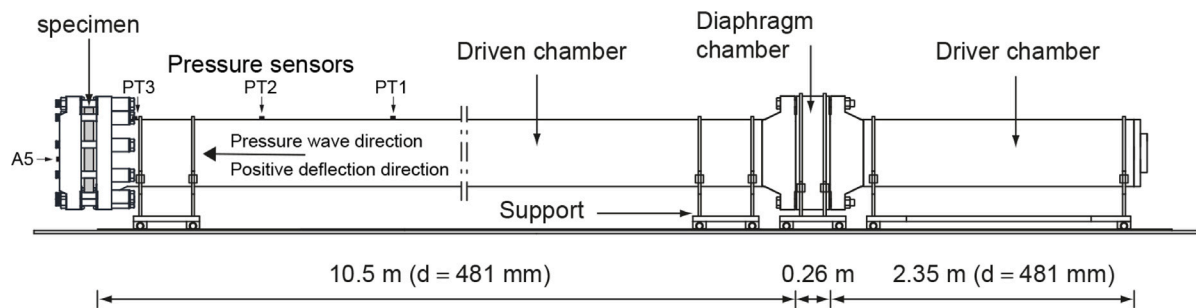

Fig. 4. Shock tube facility at the Politecnico di Milano (reprinted with permission from Elsevier, [23] edited with the initial shock wave direction and the positive measurement direction of the accelerometers).

Table 3
Initial conditions inside the shock tube chambers during the two sets of experiments (* absolute pressure values).

Experiment type	Driver Pressure* (bar)	Gas	Diaphragm Pressure* (bar)	Gas	Driven Pressure* (bar)	Gas
Low-pressure (LP)	5.4	Helium	3.2	Helium	1.01	Air
High-pressure (HP)	15	Helium	8	Helium	1.01	Air

Fig. 5 displays the pressure–time history curves recorded for each test using sensor PT3 (the closest to the specimen). The first sharp increase in pressure on the graph corresponds to the incident wave (commonly referred to as incident pressure), while the second increase represents the reflected wave (commonly referred to as reflected pressure). Low-pressure tests have a desired maximum value of the reflected pressure of about 0.4 MPa, while the amplitude of the reflected pressure for high-pressure tests is about 1.2 MPa. Due to a temporary malfunction in the setting of the inlet pressure for the driver chamber, the actual pressure in the driver chamber was higher during the LAY(1)-LP test compared to the other tests. This justifies the difference in pressure history between the LAY(1)-LP test and the others, as shown in Fig. 5a.

The loaded area of the specimens has a diameter of about 480 mm. Bolts clamped the specimen between two support lines consisting of two steel crowns. The resulting support condition is simply supported, and the diameter of the support line is 550 mm. Besides the specimen dimensions, Fig. 1 presents the loading and support conditions. The specimens were clamped between the crown at the end of the shock tube and the crown on the end part. Ten hand-tightened bolts M52 connected this end part to the rest of the shock tube. The bolts were tightened manually to a minimal torque to prevent internal stresses and damage within the specimen and to guarantee its deformability.

The pressure histories differed between the LP and HP tests (see Fig. 5). During the LP tests, the mean amplitude of the reflected peak pressure recorded was 0.43 MPa, ranging from 0.39 MPa to 0.50 MPa. In the HP tests, the mean amplitude was 1.25 MPa, ranging between 1.21 MPa and 1.28 MPa. The pressure decreases slowly, especially in the case of the LP experiments, where negative pressures occurred only after approximately 30 ms. Under high pressure, negative pressures already occurred around 15 ms after the beginning of the pressure wave. The corresponding impulses are computed as the time integral of the pressure wave multiplied by the loaded area. The considered duration of the test spanned from the beginning of the shock wave up to the first negative reflection or until 25 ms. The impulse recorded during the LP tests ranged from 0.48 kN s to 0.78 kN s, while the impulse of the HP experiments was between 1.03 kN s to 1.15 kN s. Interestingly, the impulse scattered more than the maximum pressure. The reason could be that the diaphragm's failure ruled the maximum pressure while the specimen's response governed the impulse. The pressure is almost perfectly adjustable as the diaphragms were manufactured with elevated machine precision. By contrast, the specimens were cast
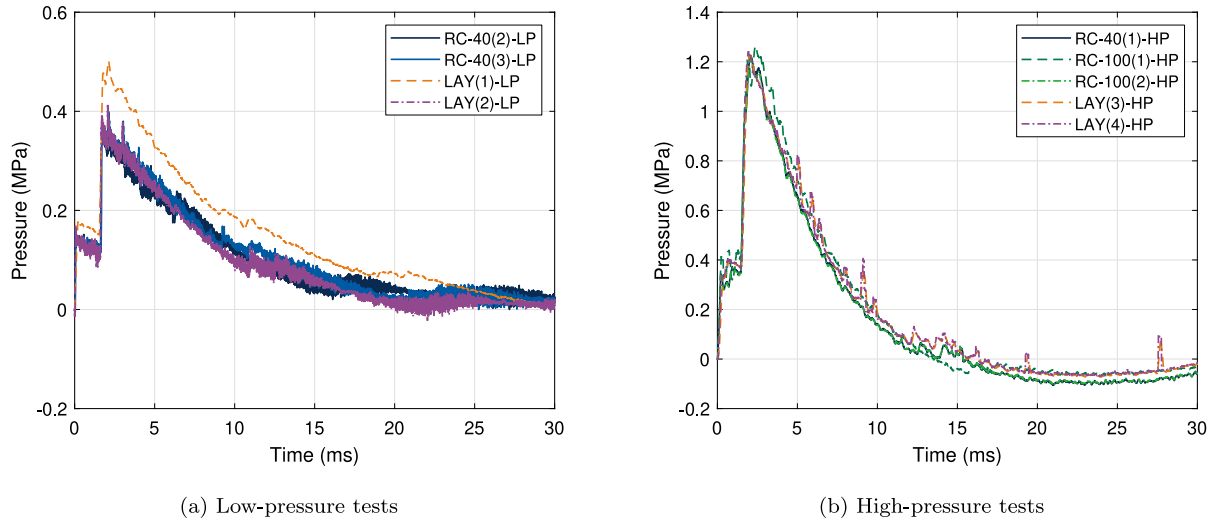
(a) Low-pressure tests

(b) High-pressure tests

Fig. 5. Temporal evolvement of the pressure in the low- and high-pressure tests.

Table 4
Overview over the specimens and the respective loading conditions.

Specimen ID	Age (d)	Peak pressure (MPa)	Impulse (kNs)
RC-40(1)-HP	65	1.22	1.04
RC-40(2)-LP	330	0.39	0.52
RC-40(3)-LP	331	0.41	0.55
RC-40(4)-LP	330	0.31	0.32
RC-100(1)-HP	69	1.26	1.15
RC-100(2)-HP	70	1.21	1.03
LAY(1)-LP	112	0.50	0.78
LAY(2)-LP	114	0.41	0.48
LAY(3)-HP	119	1.28	1.13
LAY(4)-HP	119	1.27	1.14

Fig. 6. Positions of the accelerometers on the rear side of the specimen (dimensions in mm).

manually, and their precision was inferior. Table 4 presents details of the specimens and the respective loading conditions. The specimens are labeled corresponding to their type (RC-40, RC-100, or LAY) followed by a subsequent numbering for nominally identical samples, e.g., (1), and the applied pressure state (LP for low pressure or HP for high pressure).

Three 40 mm thick RC specimens and two layered specimens were subjected to low pressure (see Fig. 5(a)). The low pressure was not applied to the 100 mm thick RC specimens, as they remained undamaged even after high-pressure tests. High pressure was applied to one 40 mm thick and two 100 mm thick RC specimens, and to two layered specimens (see Fig. 5(b)). The HP test with the 40 mm thick RC specimen was not repeated as the high loading magnitude led to the complete destruction of the tested specimen.

2.4. Instrumentation

A set of three Integrated Circuit Piezoelectric (ICP) dynamic pressure transducers was aligned along the tube axis, as shown in Fig. 4. The transducers (PT1–PT3) feature a quartz sensing element with a full-scale pressure of 6.9 MPa, a sensitivity of 0.7 mV/kPa, a rise time lower than 1 µs, and a resonant frequency higher than 500 kHz. Signal conditioning for the pressure transducers was carried out using an ICP signal conditioner with a gain of one, a bandwidth of 10 kHz, and a broadband electrical noise level of 3.5 µVrms. All channels were recorded by a single data acquisition system that supports 56 parallel channels, with a sampling rate of 1 MS/s per channel and a resolution of 14 bits. Data acquisition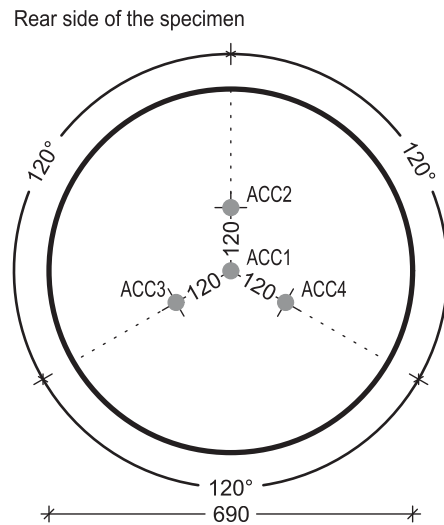 for all channels was initiated by the signal from the first pressure transducer in the tube (PT1, as shown in Fig. 4): when the measured pressure exceeds a predetermined threshold, indicating the arrival of the shock wave, the system begins data acquisition. No filtering technique was applied to the pressure data.

Besides the pressure sensors measuring the pressure wave along the shock tube (PT1–PT3 in Fig. 4), four accelerometers (ACC1–4) were glued on the specimens, one in the center and the other three 120 mm away from the center under 120° from one another, as shown in Fig. 6. An additional accelerometer was used to track the rigid body motion at the end of the last shock tube part clamping the specimen (A5 in Fig. 4).

A high-pass filter with a 100 Hz cutoff frequency filtered the retrieved accelerations. The cutoff frequency was chosen to remove the low frequencies seen in the fast Fourier transform (FFT) analysis (see Figs. 22 and 23). Integrating the filtered accelerations once yields the velocities of the respective specimen position or the shock tube. Another integration of the velocity results in the shock tube or specimen displacement data.

The acceleration, velocity, and displacement are defined as positive if the accelerometer moves in the direction of the shock wave. The
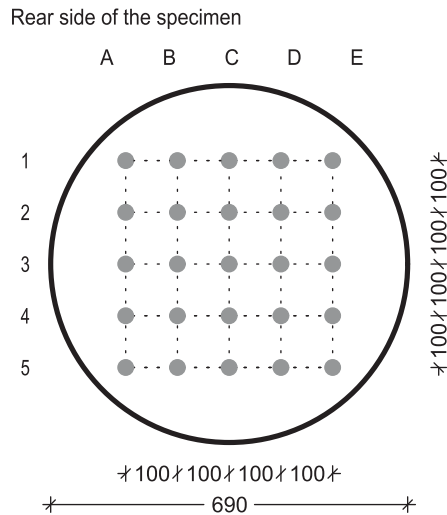
Rear side of the specimen

Fig. 7. Measurement positions of the UPV measurements (dimensions in mm).

accelerations displayed and used for the integration to velocities and deformations were filtered and cut at the value of the measurement limit of the instrument, which is 500 *g*, where *g* represents the gravitational acceleration. Moreover, the maximum values were determined until 30 ms after the shock wave passed the pressure gauge.

2.5. Interface analysis

Two different techniques, ultrasonic pulse velocity (UPV) and direct pull-off strength test, were used to assess the interface, i.e., the bond between the layers of the layered specimens. The map of the positions for the UPV measurements can be found in Fig. 7. If the specimens had voids or bonding issues, the UPV would register a subpar value due to the extended time for the signal to pass through the specimens.

Furthermore, the pull-off bond strength indicates whether the tensile failure occurs in the interface between the different layers or within the weakest layer. The pull-off bond tests were carried out on the layered slabs after the low-pressure tests, after which the specimens were undamaged. The corresponding diameter for the pull-off bond tests was 60 mm. Six tests were carried out in total. In three cases, the drilling started on the top side of the specimens up to the intermediate ILC layer to assess the bond quality between the SHLC[3] and the ILC. In the other three experiments, cores were drilled starting from the bottom side of the specimen with the C35/45 concrete layer, specifically investigating the bond between the C35/45 and the ILC.

3. Results

3.1. General behavior of the specimens

During the low-pressure tests, a fine and symmetric crack pattern evolved on the blast-far side of the RC-40 specimens as a consequence of bending raised by the loading and support conditions. The individual cracks were fine, having a width between 0.05 mm to 0.3 mm as displayed in Figs. 8(a), 8(b), and 8(c). The crack patterns differed quite strongly, especially regarding the number of cracks occurring. While experiment RC-40(4)-LP (see Fig. 8(c)) resulted in very few cracks, the cracking pattern of specimen RC-40(3)-LP (see Fig. 8(b)) was very dense. The crack width in the RC-40(4)-LP specimen was even slightly smaller with widths of up to 0.2 mm, indicating that the damage was less severe. These differences could be related to the different maximum

pressures. While RC-40(4)-LP was loaded with a maximum pressure of 0.31 MPa, the maximum pressure on RC-40(3)-LP was 0.41 MPa. Both the maximum loading pressure of 0.39 MPa and the rear-side crack pattern of specimen RC-40(2)-LP ranged between that of the other two experiments. The maximum pressure and the corresponding impulses are also displayed in Table 4.

In contrast to the low-pressure experiments, the high-pressure loading of the 40 mm thick RC slab led to the complete fragmentation of the slab with debris that was smaller than 10 mm × 10 mm × 10 mm. Fig. 8(d) illustrates that besides the destruction of the concrete matrix, the internal steel reinforcement was completely bent after the experiment.

The RC-100 specimens developed a single vertical crack during the assembly of the shock tube facility due to imperfections in the casting process. This crack appeared on the specimen's front side prior to the test, experiencing compressive stresses during the blast test, potentially impacting the slab's stiffness and altering its deformations. No additional cracks or damage were detected after the completion of the blast test.

Fig. 9 shows the backside crack patterns of the layered specimens after high-pressure experiments. Generally, the crack pattern was similar to that of the RC-40 counterparts tested with low pressure. However, the number of cracks was smaller than in the case of the RC-40 specimens, and the crack width was even finer with maximum widths of only 0.1 mm. Unlike in the case of the RC-40 specimens, a difference between the crack patterns of two layered specimens was not present. Neither the number of cracks nor the width varied. A reason for that could be that the maximum loading pressures were also very similar in these two experiments, 1.28 MPa in the case of specimen LAY(3)-HP and 1.27 MPa in the case of specimen LAY(4)-HP.

All in all, the crack patterns verified that the layered specimens suffered minor damage at a threefold higher pressure than the RC-40 specimens. The layered specimens remained undamaged under LP conditions without any visible cracks. In the case of HP loading, however, the damage observed for the layered specimens was higher than that of the RC-100 specimens. The higher bending capacity and mass of the RC-100 compared to the LAY specimens could explain the differences in the damage extent.

3.2. Specimen acceleration

Two observations stood out when looking at the acceleration measurements in Fig. 10. Firstly, accelerations started earlier under HP than under LP. Secondly, the loading pressure and the specimen's stiffness governed the decay of the accelerations after the impact. Under low pressure, the decay of the layered specimens was substantially faster than that of the RC-40 slabs (see Fig. 10(a)). However, the amplitudes of the accelerations always exceeded the accelerometer's measurement limit of 5,000 m/s². The oscillation period of the RC-40 was also longer than that of the layered specimens.

Under high pressure, the oscillations of the layered and RC-100 slabs endured longer than those of the layered slabs under low pressure, but the amplitudes decreased quicker than those of the RC-40 counterparts under LP (see Fig. 10(b)). The initial response of the layered specimens differed from that of the RC-100 slabs. The maximum acceleration of the layered ones occurred right at the beginning of the loading and then started to decay. By contrast, the maximum accelerations of the RC-100 slabs occurred after an initial phase of inclining amplitudes of the vibration. Nevertheless, the following decay resembled that of the layered slabs. In both cases, the pressure abated about 15 ms after the beginning of the pressure wave. The RC-40 specimens experienced high acceleration amplitudes until approximately 11 ms after the beginning of the pressure application. At this point, the pressure wave already destroyed the specimens. The comparison of the maximum accelerations of all accelerometers attached to the specimen shows that all specimens experienced accelerations that exceeded the capacity of the accelerometers. Hence, the maximum accelerations cannot be compared as the actual acceleration amplitudes remain unclear.
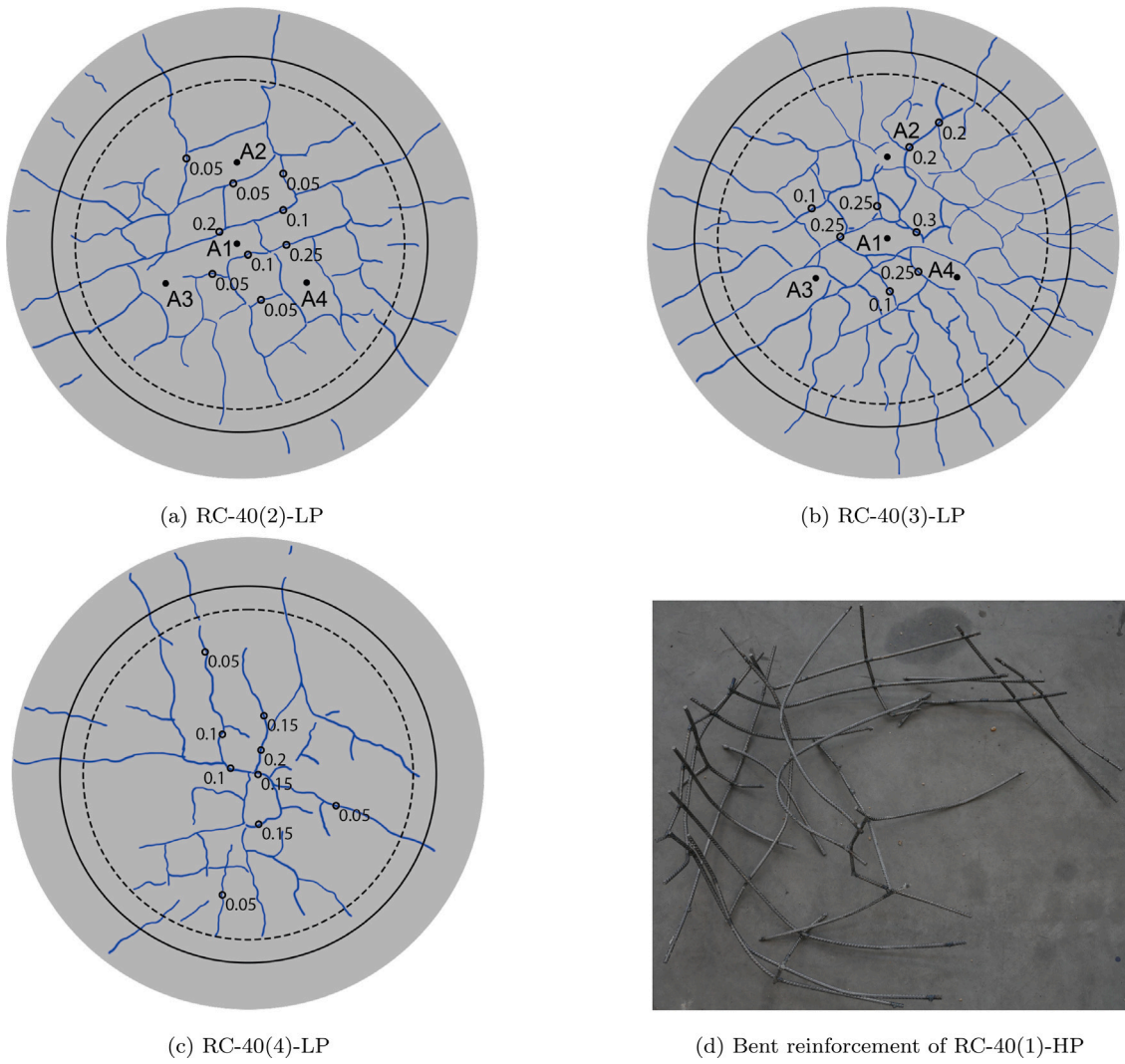
(a) RC-40(2)-LP

(b) RC-40(3)-LP

(c) RC-40(4)-LP

(d) Bent reinforcement of RC-40(1)-HP

Fig. 8. Back side crack pattern and damage of the RC-40 specimens after low- and high-pressure tests (crack widths in mm).

(a) LAY(3)-HP

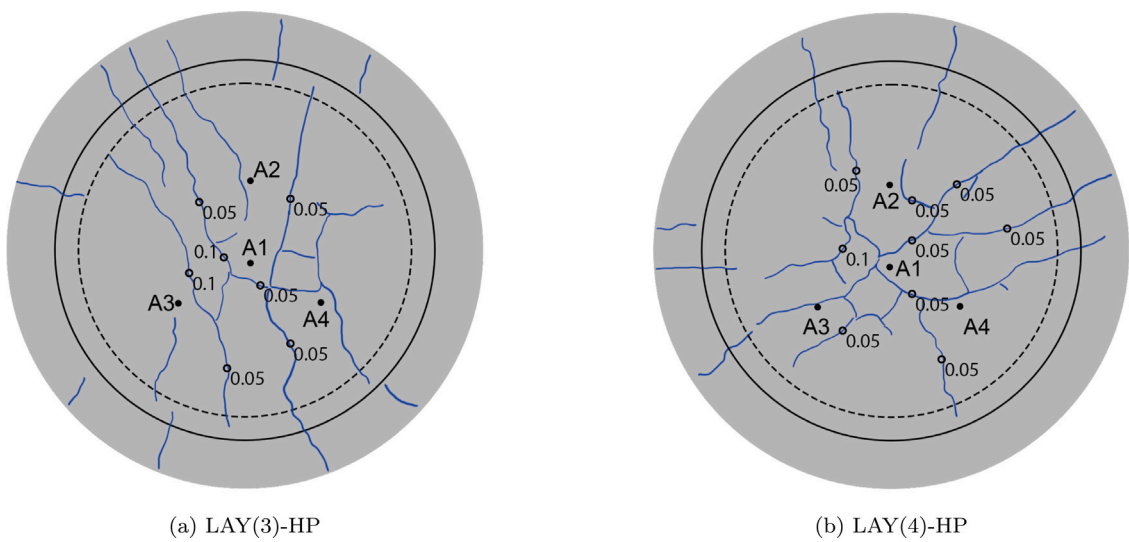(b) LAY(4)-HP

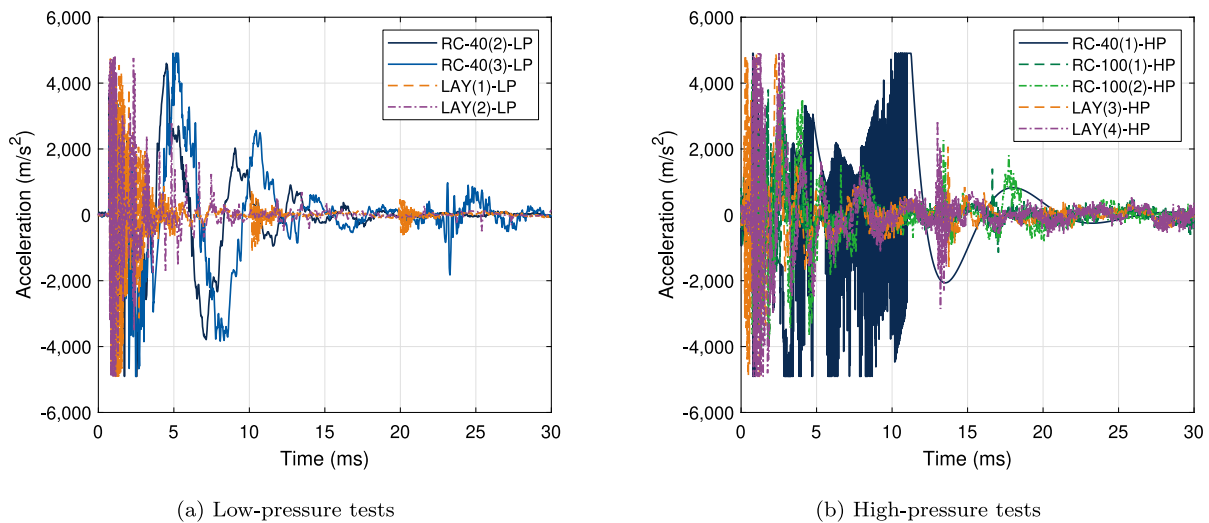**Fig. 9.** Back side crack pattern of the layered specimens (LAY) after the high-pressure tests (crack widths in mm).

(a) Low-pressure tests

(b) High-pressure tests

Fig. 10. Accelerations in the middle of the specimens (measurements of ACC1).

(a) Low-pressure tests

(b) High-pressure tests
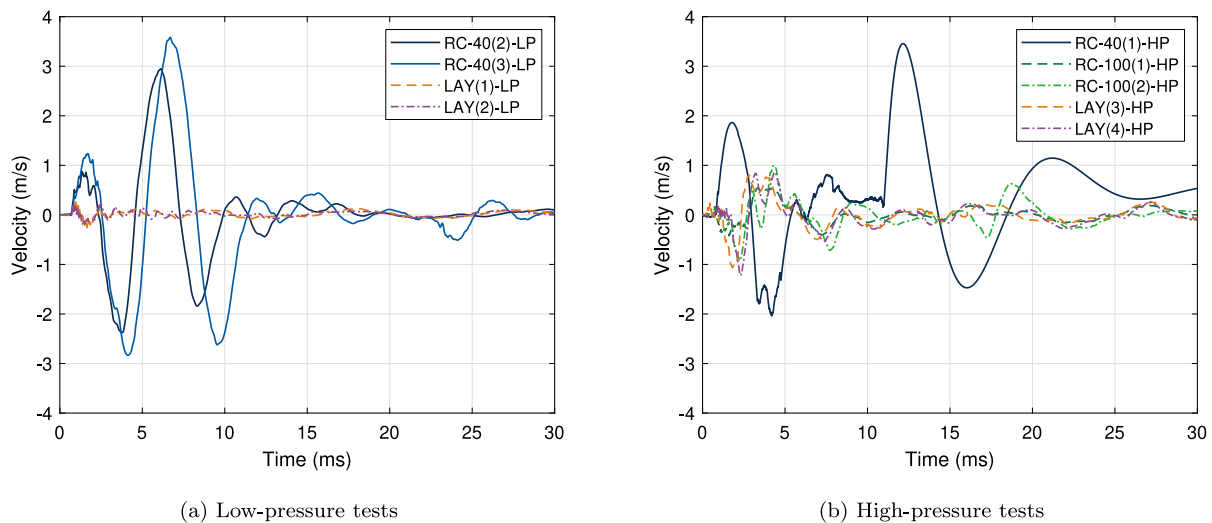
Fig. 11. Velocities in the middle of the specimens (measurements of ACC1).

3.3. Specimen velocity

The assessment of the velocities, obtained by integrating the measured accelerations, allows a more robust comparison among the different structural behavior of the specimens (see Fig. 11). The first look proves that the RC-40 samples' maximum and minimum velocities, i.e., the oscillation's amplitude, distinctly exceeded the other samples' velocities under both pressure conditions. In addition, the duration of the oscillations was more elevated. Under low pressure (see Fig. 11(a)), the velocity amplitude of the layered samples was less than 0.3 m/s, while the RC-40 samples reached velocity amplitudes of up to 3.6 m/s. The amplitude of the first oscillation was smaller than that of the second positive peak in the case of the RC-40 slabs. At first, a lower-amplitude pressure plateau reached the specimen (see Fig. 5), leading to a positive velocity in its direction and pre-damage. This pressure wave was reflected as a recurring suction wave inducing negative velocities. Finally, this wave returned as compressive in the original blast direction, causing positive velocities.

Under high pressure (see Fig. 11(b)), the velocity amplitudes of the layered and RC-100 samples were around 1.0 m/s, while the RC-40 specimens attained up to 2.0 m/s. The oscillation period and the time

frame for the major velocity decay of the layered and RC-100 samples were very similar. While the RC-40 specimens had high positive velocities at the beginning, the other samples immediately deformed in the negative direction, which is the direction opposite to the shock wave. The first compressive wave probably did not generate velocity and deformation of the specimens with the higher bending stiffness. However, the suction wave pulled the specimens in the opposite direction to that of the high bending resistance, where the rebars would be on the tensile side, which could lead to pre-damage that reduced the resistance to the second returning compressive wave. Hence, the velocities and deformations were higher due to the suction wave and the returning compressive wave.

Fig. 12 shows the maximum absolute velocities of the different samples as a function of the input pressure. The layered specimens featured negligible maximum velocities compared to their RC-40 counterparts under low pressure. The velocity amplitude of the RC-100 specimens was similar to that of the layered specimens under high pressure. While the velocities of the layered specimens increased with increasing pressure, the velocities of the RC-40 specimens did not. That could be due to the severe fragmentation of the RC-40 specimen under high pressure, impeding reliable acceleration measurements. All in all, the
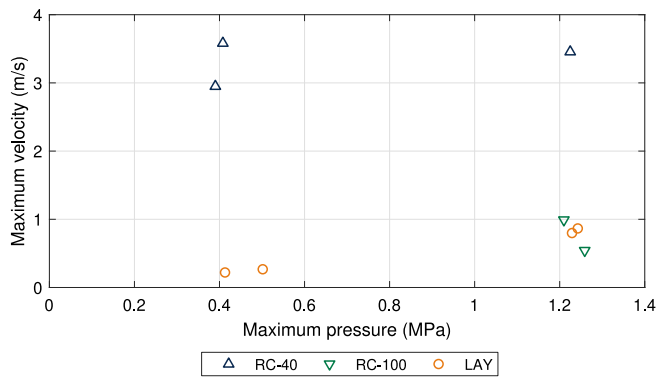
**Fig. 12.** Maximum velocities plotted against the initial pressure (measurements of ACC1).

amplitudes of the layered and RC-100 slabs were below $1.0\,\text{m/s}$, while the RC-40 specimens reached velocities of up to $3.6\,\text{m/s}$.
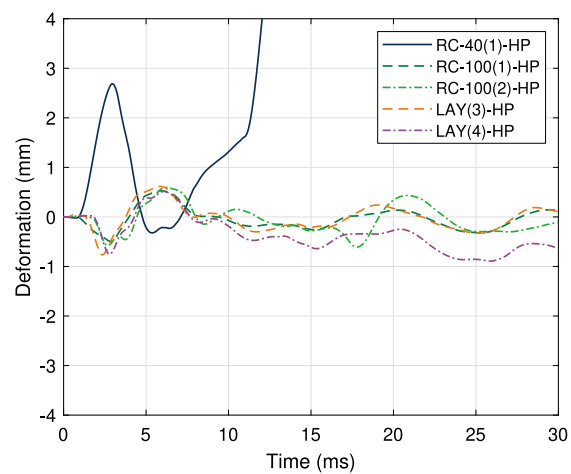
3.4. Specimen deformation

In Fig. 13, each sample's absolute deformation time histories are plotted. The specimen type played a significant role in the deformation responses of the specimens under the same pressure amplitudes. While the layered specimens hardly deformed under low pressure (see Fig. 13(a)), the oscillations of the RC-40 slabs turned out to be very high. Indeed, the deformation amplitudes reached almost $4\,\text{mm}$ in both positive and negative directions, whereas the layered specimens consistently deformed less than $0.1\,\text{mm}$ in either direction.

Fig. 13(b) displays the deformations under high pressure, and it becomes evident that the deformation of the RC-40 exceeded the deformations of both the RC-100 and the layered specimens by far, the latter pair exhibiting a very similar response. Indeed, the amplitudes of the deformations of the RC-100 and layered samples were less than $0.8\,\text{mm}$ in both directions, while the positive amplitude of the RC-40 specimens was already $2.7\,\text{mm}$ at its first peak. That already overstepped the amplitude of the first peak under the low-pressure loading. Afterward, the specimens were likely completely fragmentized, making the accelerometer readings unreliable.

It is also apparent that the RC-40 specimens experienced positive deformations, i.e., in the direction of the shock wave, before the negative ones under both loading pressures (see Figs. 13(a) and 13(b)).
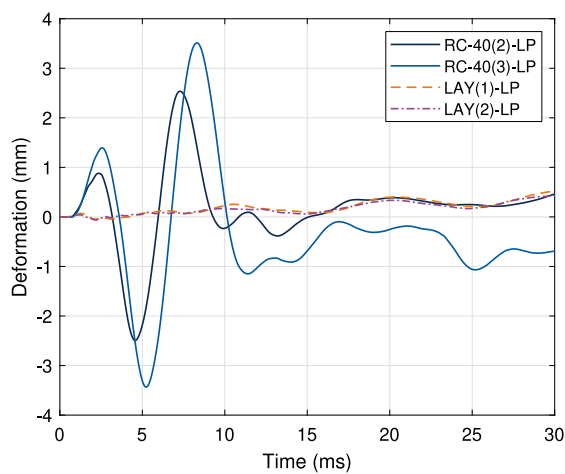
The positive deformations resulted from the compressive shock wave, while the negative ones resulted from its reflection on the specimen's free end. From that point, the wave gets reflected back and forth in the shock tube until the specimen eventually fails. This caused the oscillating deformations of the specimens. By contrast, the RC-100 and LAY specimens did not undergo positive deformations initially but only after the first negative deformations. Afterward, they were oscillating as well. The reduced bending stiffness of the RC-40 specimens seems to be the reason for the initial positive deflections when the results are compared to the ones by COLOMBO ET AL. [23]. In their analysis, the specimens, which were pre-damaged by exposure to fire and therefore had a lower stiffness, also experienced positive deflections ahead of negative ones. Moreover, the shock wave induced higher deformation amplitudes to specimens with pre-damage and, thus, lower resistance. The oscillations also decayed more slowly. Generally, it can be concluded that higher damage results in higher overall deflections.

Fig. 14 displays the maximum absolute deformations of the different samples as a function of the input pressure. Evidently, the maximum deformations of the RC-40 specimens, with amplitudes up to $3.5\,\text{mm}$ under low pressure, exceeded those of the other two specimen types by far. The layered samples experienced between $0.4\,\text{mm}$ to $0.5\,\text{mm}$ deformation under low pressure, which slightly increased under high pressure (in the range of $0.5\,\text{mm}$ to $0.6\,\text{mm}$). The RC-100 samples' deformations under high pressure resembled those of the layered specimens and fell in the same range as their layered counterparts.

3.5. Damping ratio

The damping ratio ζ is derived from the decay of the acceleration, velocity, or deformation signals over time, as per Eq. (3) [24]:

$$\zeta = \frac{1}{2\pi m} \ln \frac{x_{\text{n}}}{x_{\text{n+m}}} \tag{3}$$

where x_{n} and $x_{\text{n+m}}$ represent two peaks in the free vibration response of the structure separated by m cycles. As stated in CAO ET AL. [24], the damping ratio is deemed reliable only up to a value of $20\,\%$.

Many authors reported a growth of the damping ratio with increasing internal damage, provoking friction between the cracks. This friction dissipates energy and therefore damps the specimen's response [25–28]. KIRAL ET AL. [28] studied the damping of glass-epoxy composite beams clamped on one side under impact loading. The increase in the damping ratio was attributed to friction resulting from matrix cracks and broken fibers. The damping ratio stemmed from the free vibration deformation response of the specimens after the impact tests. The
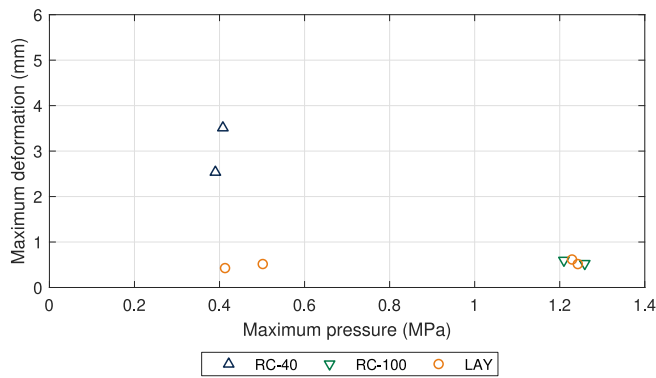

(a) Low-pressure tests

(b) High-pressure tests

Fig. 13. Deformations in the middle of the specimens (measurements of ACC1).

Fig. 14. Maximum deformations plotted against the initial pressure (measurements of ACC1).

natural frequencies were found to be identical for small damping ratios. Hence, they are poor damage parameters.

Generally, a higher damping ratio indicates a faster acceleration, velocity, or deformation decay. In this study, the damping ratio was determined at 200 ms after the blast event and was intended to provide a qualitative indicator of incipient damage in the specimens. It resulted from the decay of the specimen velocities. In fact, accurately determining the damping ratio requires a free vibration response, which is only partially achieved in our experiments at this temporal instant. In addition, the expected scatter of the data due to the highly dynamic test conditions also plays a role in the choice of the reference peaks taken into account for the calculations. These peaks were selected on a case-by-case basis in order to obtain the most representative description of the damage, excluding occasional non-realistic extreme values. Nevertheless, the damping ratios presented in Fig. 16 are intended to support an effective comparative assessment of the individual experiments, with particular reference to the performance of layered slabs. The restrictions in determining the correct damping ratio can be summed up in the following three main reasons:

1. The damping ratios were not determined in a free vibration response.
2. The damping ratio values scattered strongly.
3. The subjective choice of the peak values affects the results.

Fig. 15 displays the velocity profiles of an RC-40 and a LAY specimen with the respective chosen peaks that were used to determine the damping ratio. The damping ratio was always determined between either three or four subsequent velocity peaks.

Fig. 16 presents the damping ratios of the individual experiments. Firstly, the high scatter of the damping ratios is attributed to the wide scattering in the accelerations, the subjective choice of the relevant pairs of peaks, and the intrinsic scattering of the material properties and, therefore, the slabs' behavior. The damping ratio of the RC-40 slabs subject to the same loading pressure partly diverged up to 2.8 %.

In contrast to the findings of other researchers, increased damage due to increasing loading pressures did not increase the damping ratio. Instead, the damping ratio values of the layered specimens support the finding of the pronounced scattering. The layered specimens exhibited damping ratios between 0.8 % to 3.1 % under the low loading pressure. The higher value was measured in an experiment where the velocities decayed faster than in other cases. Hence, the damping ratio was determined about 50 ms earlier than in all other cases, around 150 ms after the shock wave reached the specimen. Under the high loading pressure, the value scattered less and ranged between 1.1 % to 1.7 %.

Under the low loading pressure, the RC-40 specimens' damping ratio was about four times higher (between 4.1 % to 6.9 %) than that of the layered specimens. Under the high loading pressure, the damping ratio

of the RC-100 specimens exceeded that of the layered specimens by about three times. Both values were about twice as high as that of the layered specimens and fell in the range of 3.8 % to 4.3 %.

Considering the limitations mentioned above regarding the quantitative values of the damping ratios, the only conclusion of the damping ratio evaluation is that the damage indicated by the percentage of the damping ratio to the layered specimens was lower than that of the RC-40 and RC-100 options under equivalent loading conditions. However, the scattering of the values impedes further conclusions.

3.6. Relative speed of sound

The relative speed of sound c_{rel} was computed as the ratio between the UPV values measured before and after the tests:

$$c_{rel} = c_{after}/c_{before} \tag{4}$$

where c_{after} is speed of sound measured after the experiments, and c_{before} is that measured before the experiment.

The relative speed of sound determined with Eq. (4) is an indicator of the internal damage of the specimens. Indeed, if the concrete crushes or cracks, the relative speed of sound decreases as the elastic modulus declines [29,30]. Likewise, if the layered specimens experienced debonding due to high shear stresses or due to the tensile wave reflected at the interface between the layers resulting from the impedance difference between them, the relative sound speed would also decrease.

In the case of the two 100 mm thick RC specimens (see Fig. 17), the relative UPV decreased by 10 % due to the shock wave loading. The UPV values were consistently uniform across the entire slab area (refer to Fig. 7 for the measurement positions), indicating that no local defects affected the measurements. The small standard deviations support this observation. In particular, the crack due to the support constraints did not result in a local change of the UPV, as the small standard deviation in Fig. 17 proves. On the contrary, internal microcracks likely affect the global stiffness of the sample and, therefore, the specimen's speed of sound.

The layered specimens exhibited degradation of the UPV of 1 % under the low pressure and of 2 % to 3 % under the high pressure (see Fig. 17). Thus, the low- and high-pressure experiments hardly damaged specimens. Neither severe damage nor debonding of the three different layers occurred. Moreover, the UPV degradation was smaller than that of the two 100 mm thick RC specimens. That indicates that less microcracking likely occurred in the case of layered specimens. However, the standard deviation of the relative speed of sound over the area of the layered slabs exceeded that of the RC-100 slabs.

In particular, the second layered specimen subject to the low pressure (LAY(2)-LP) had a coefficient of variation of around 22 %. However, looking at the individual values of the UPV, it is evident that the high standard deviation comes from only one value that falls out of range. Hence, the mean value can be trusted. The UPV value falling out of range of one of the layered specimens under the low loading pressure was not linked to the high value of the damping ratio under the low loading pressure (see Fig. 16). The suspiciously high value of the damping ratio occurred in the case of the second specimen with the low standard deviation. Hence, both values are not interconnected and do not seem to have a physical meaning. Thus, such outliers must be handled carefully and should not be overinterpreted.

3.7. Pull-off bond tests

To further investigate the damage of the layered specimens after the experiments, a series of pull-off bond tests was performed on the two slabs subjected to low pressure blast. The UPV measurements have confirmed that there was no degradation observed in the layered specimens after the blast testing, indicating an absence of cracking or bond failure. In the case of specimen LAY(1)-LP, the pull-off tests were carried out from the side of the SHLC³ cover layer, while the pull-off
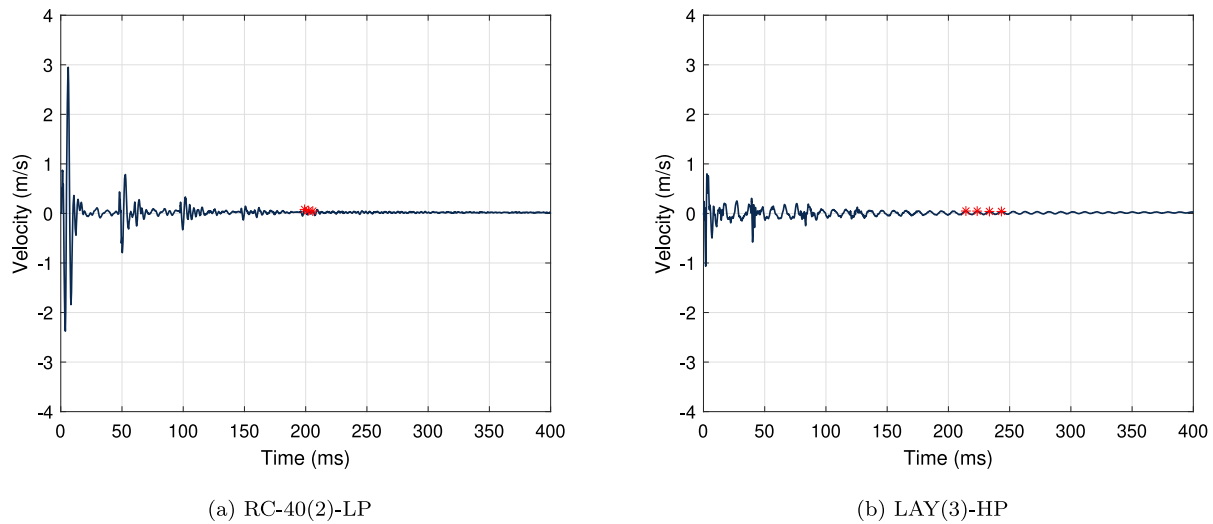
(a) RC-40(2)-LP

(b) LAY(3)-HP

Fig. 15. Velocity profile and peaks used to determine the damping ratio, the respective peaks are marked with red asterisks (measurements of ACC1).
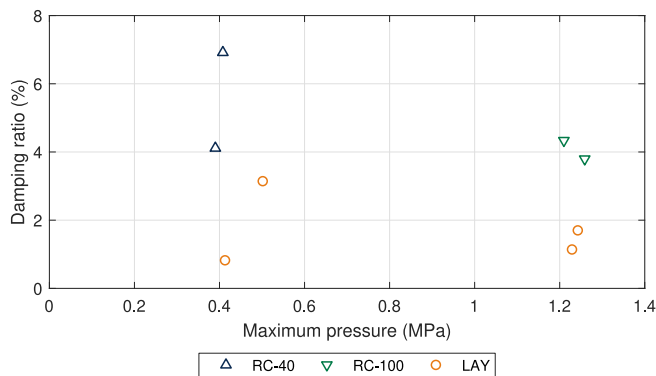

Fig. 16. Damping ratios plotted against the initial pressure (measurements of ACC1).

Table 5
Pull-off strength of the layered specimens.

	Pull-off strength (MPa)			
	1	2	3	Mean
SHLC³ - ILC	0.9	0.9	0.8	0.9
ILC - C35/45	1.4	1.4	1.6	1.5

was carried out from the side of the C35/45 base plate in the case of specimen LAY(2)-LP. Therefore, the bond between the SHLC³ and the ILC layer was the focus when examining the first specimen, while the bond between the ILC layer and the C35/45 was assessed in the case of the second specimen. In both cases, the failure occurred within the ILC damping layer close to the interface with the SHLC³ or C35/45, respectively, and the measured values actually correspond to the tensile strength of the ILC. As a result, the bond strength between SHLC³ and ILC exceeded 0.9 MPa, and the bond strength between the ILC layer and the C35/45 must be higher than 1.5 MPa. Table 5 shows the strength values obtained for each single test and proves that the scattering was small.

The reason why the lower bound of the bond strength determined in the SHLC³ and ILC interface was smaller than the lower bound of the bond strength in the ILC and C35/45 interface can be seen in Figs. 18 and 19. It is clear that there are more lightweight aggregates in the fracture surface in the case of the bond tests between SHLC³ and ILC (see Fig. 18) than in the fracture surface in the case of the bond tests between ILC and C35/45 because the mortar was denser than the

aggregates and flowed down toward the C35/45 layer (see Fig. 19). Because of the minor tensile strength of the aggregates compared to the cementitious matrix, the bond strength determined in the ILC and C35/45 interface was higher.

Interestingly, both the determined minimum bond strengths, i.e., the material strength of the ILC layer, exceeded the strength determined by direct tensile testing of dog-bone-shaped specimens, which was only 0.3 MPa. That could be due to several reasons. First, the production mode may have affected the hardened properties of the ILC, i.e., laminating large plates is less prone to defects than casting into small molds. Second, the size effect likely played a major role, as the dog-bone-shaped specimens were substantially longer, and the possibility of inherent defects was higher. In addition, even small eccentricities of longer specimens also lead to bending stresses, as proven by Cattaneo and Rosati [31].

4. Discussion

4.1. Symmetry of the specimens' response

Fig. 20(a) proves that the deformations along the three outer positions (ACC2–4) of the RC-40 specimen (see Fig. 6) were very similar and lower than the deformation in the center of the slabs (ACC1), as expected. According to Colombo et al. [23], this symmetric profile of deformations results from the planarity of the shock wave.

However, this consideration does not hold true when looking at the other specimen types, i.e., the RC-100 (see Fig. 20(b)) and the layered slabs (see Fig. 21), where the deformations measured in the center were not necessarily the highest. Moreover, the deformations of the peripheral accelerometers, which were equally distant from the center, were not mutually alike. Although the localized measurement strongly influences the measured value and very small deformation amplitudes were observed, this distinct behavior could also suggest a more important role played by a higher vibration mode, where the maximum deformation does not necessarily occur in the center of the specimen. Another possible reason could lie in the asymmetric crack pattern detected for these specimens. However, the crack patterns were generally symmetric.

4.2. Bond properties of the layered samples

The bond strength between the SHLC³ and the ILC layers and between the ILC and the C35/45 layers were found to be uncritical, as both bond strengths exceeded the tensile strength of the ILC layer.
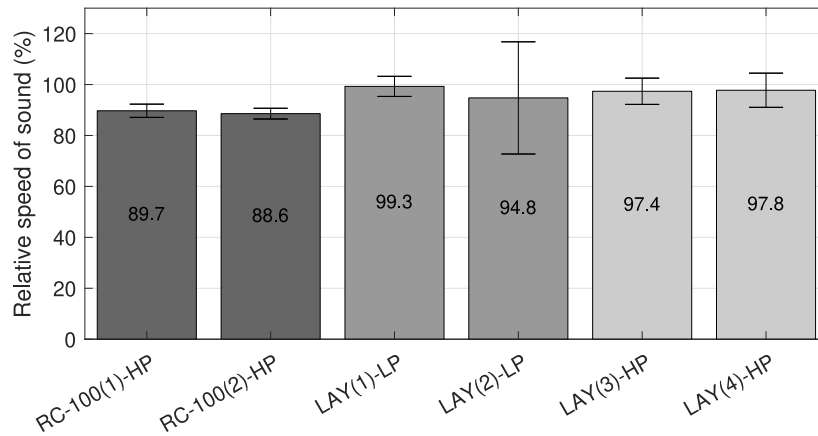
Fig. 17. Relative speed of sound of the RC-100 and layered specimens after the experiments.

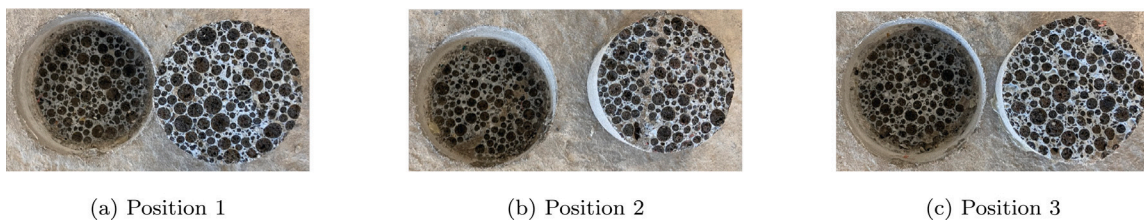(a) Position 1

(b) Position 2

(c) Position 3

Fig. 18. Fracture surfaces of the drill cores of the pull-off bond experiments on the interface between the SHLC³ and the ILC interface.
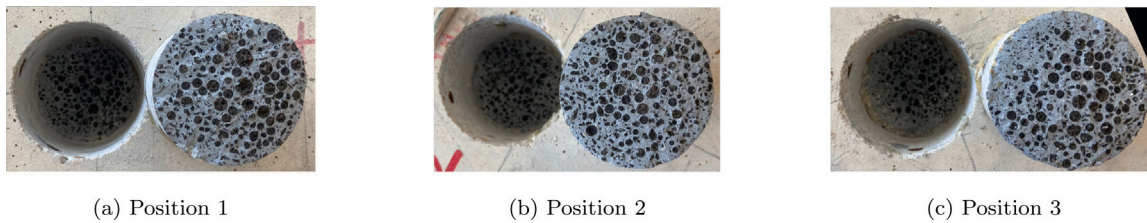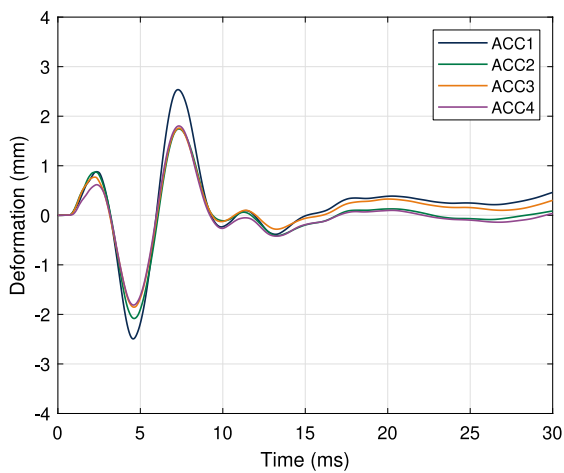

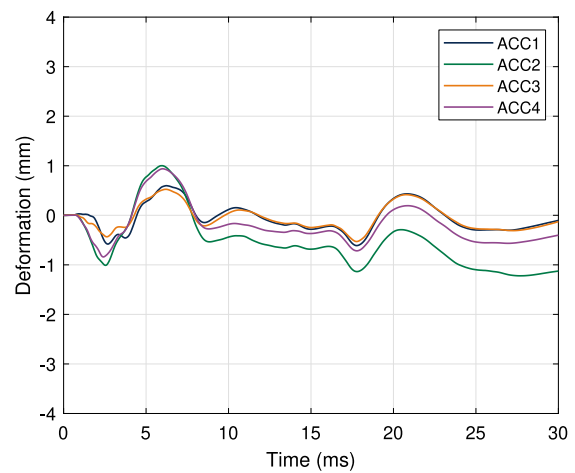(a) Position 1

(b) Position 2

(c) Position 3

Fig. 19. Fracture surfaces of the drill cores of the pull-off bond experiments on the interface between the ILC and the C35/45 interface.

(a) RC-40 specimen under low pressure

(b) RC-100 specimen under high pressure

Fig. 20. Comparison of the deformations from all four accelerometer measurements of (a) one RC-40 and (b) one RC-100 specimen.

(a) Layered specimen under low pressure

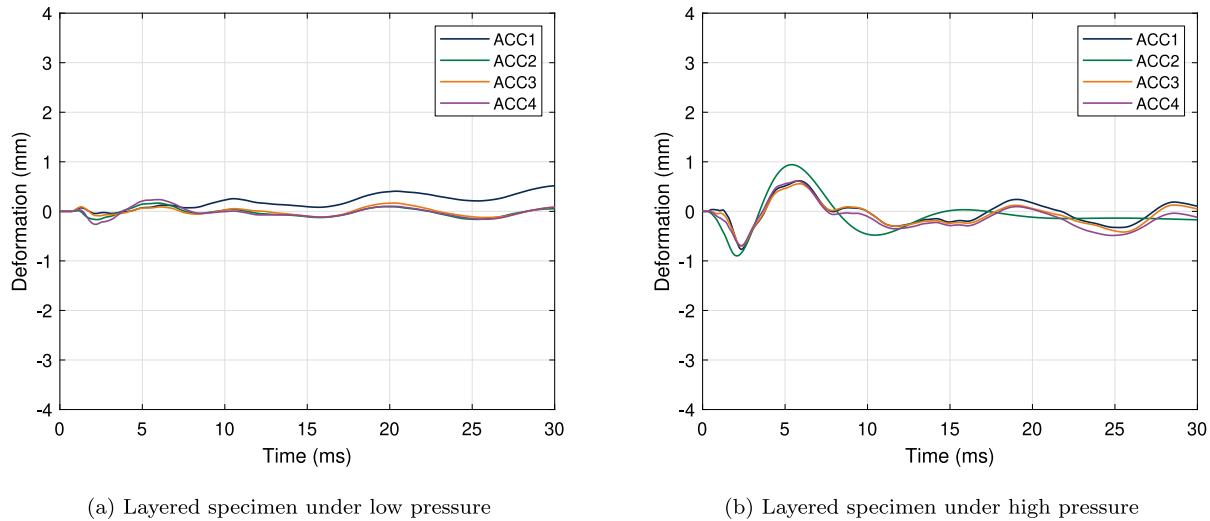(b) Layered specimen under high pressure

Fig. 21. Comparison of the deformations from all four accelerometer measurements of one layered specimen under (a) low pressure and (b) one under high pressure.

Thus, failure was more likely to occur within the ILC layer than in the interface between the layers. Moreover, the UPV proved that neither the material nor the bond deteriorated due to the blast experiment. That means that the returning tensile reflection of the shock wave was uncritical, as its amplitude remained below both the bond strength and tensile strength of the weakest material. Therefore, the layered specimens acted like a solid body instead of behaving like three individual parts. That is essential for determining the theoretical bending stiffness and the eigenfrequency and for achieving an enhanced and robust protective action of the externally bonded damping and strengthening layer on the concrete element.

4.3. Frequency response of the specimens

Figs. 22 and 23 present the FFT of the high-pass filtered acceleration signals of the different slabs. In many cases, ACC3 showed anomalous peaks at frequencies around 120 Hz, which are regarded as clear measurement errors and neglected in the discussion. The theoretical eigenfrequency of the RC-40 slabs is 463.4 rad/s and the corresponding frequency is 73.7 Hz, while the actual main frequencies under the low-pressure loading (see Fig. 22(a)) fell in the range of 164 Hz to 174 Hz, which was double of the theoretical frequency. Again, the theoretical eigenfrequency of the RC-100 slabs is 1,177.6 rad/s with a corresponding frequency of 187.4 Hz, while the experimentally visible eigenfrequencies under the high pressure (see Fig. 22(b)) were in the range between 83 Hz to 1,292 Hz. A distinct individual eigenfrequency could not be concluded, although one of the two specimens had a clear peak in the FFT signal at a frequency of 1,167 Hz.

The theoretical eigenfrequency of the layered slabs of 1,156.4 rad/s and the associated frequency of 184.0 Hz were also not distinct in the FFT plots. Under the low pressure, one specimen had a peak at 931 Hz, and the other one had a peak at a higher frequency of 1,758 Hz. Hence, both peaks were more than five times higher than the theoretical frequency. A frequency band between 269 Hz to 931 Hz appeared in the measurements. Under the higher pressure, the layered specimens showed a frequency band between 80 Hz to 516 Hz with more dominant peaks between 494 Hz to 516 Hz. Thus, they were more than double the theoretical values.

The relatively long loading duration of the pressure waves may prevent the slabs from free vibration, forcing their oscillation to some extent. That could be the reason for the non-distinctive eigenfrequencies. Assuming a loading duration of 20 ms, the corresponding load

frequency would be 50 Hz. The load frequency would be 100 Hz for a loading duration of 10 ms. Moreover, the overall movement of the shock tube could affect the measured frequencies and lead to the frequency bands.

Eigenfrequencies are also governed by the mass and the bending stiffness of the samples, and these properties are dealt with individually in the following.

### 4.4. Influence of the specimen's mass and inertia

The specimen type strongly affected the specimen's mass (see Table 1), which, in turn, has a significant influence on its oscillation behavior, i.e., the eigenfrequency. The mass, and, hence, the inertia, of the RC-100 slabs was almost 20 % higher than that of the layered specimens, which could be the reason for the small accelerations of the RC-100 samples in the initial loading stage. Moreover, the RC-100 slabs experienced a higher damping ratio and, thus, a faster decay of the loading.

The RC-40 specimens' mass was almost 50 % smaller than the layered specimens'. That increases the decay time of the RC-40 specimens. Nevertheless, the general shape of the acceleration signals of the two variants under the low loading pressure was similar. However, the frequency of the main movement of the RC-40 specimens was minor.

4.5. Influence of the bending stiffness

The bending stiffness should affect the deformations under a particular loading condition. Fig. 11 and Fig. 13 prove a clear difference between the velocities and deformations of the RC-40 slabs compared to the layered slabs under low pressure. The bending stiffness of the RC-40 specimens was only 8 % of that of the layered specimens. In turn, the amplitudes of the deformations of the layered specimens were only about 12.3 % to 20.5 % of those of the RC-40 slabs. The relative velocity amplitudes were in the range from 6.1 % to 9.3 %.

Although the stiffness of the RC-100 specimens was more than 20 % higher than that of the layered slabs, the deformation and velocity amplitudes were almost identical. The higher stiffness of the RC-100 specimens compared to the layered ones could also be the reason for the smaller relative UPV. Due to the higher stiffness, the deformations led to higher stresses in the case of the RC-100 slabs. Hence, they could have led to more substantial damage.
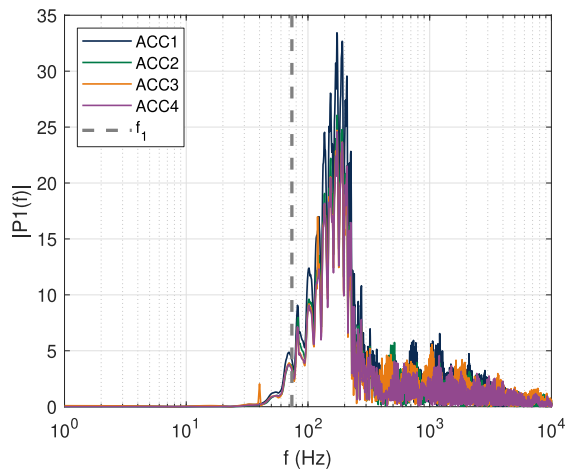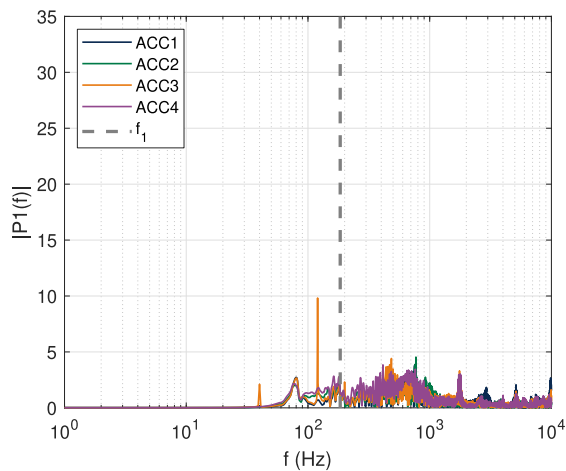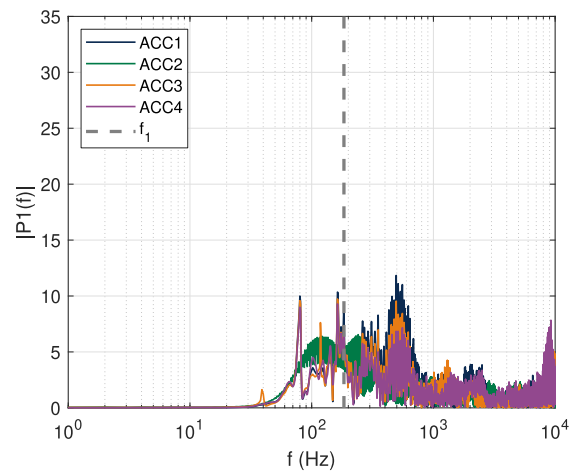
(a) 40 mm thick RC slab under the low pressure
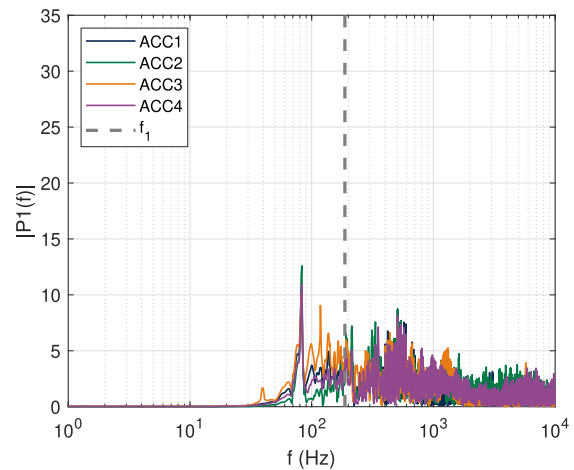
(b) 100 mm thick RC slab under the high pressure

Fig. 22. FFT of the acceleration measurements of the plain RC slabs with the lowest theoretical eigenfrequency values f_1 in gray.

(a) 100 mm thick layered slab under the low pressure

(b) 100 mm thick layered slab under the high pressure

Fig. 23. FFT of the acceleration measurements of the layered slabs with the lowest theoretical eigenfrequency values f_1 in gray.

5. Summary

The experimental investigation's primary objective was to assess the performance of a layered retrofitting solution under blast-induced pressure loads. Previous studies have demonstrated the effectiveness of such an approach against localized and severe impacts [15]. The experimental results revealed that the 40 mm thick reference samples suffered significant damage in low-pressure tests, showcasing a dense crack pattern with residual crack openings of up to 0.3 mm following the test. After the high-pressure test, the 40 mm thick reference specimen was completely fragmentized. In contrast, the layered solution demonstrates notably superior behavior during both low- and high-pressure tests. Remarkably, it exhibited no cracks after the low-pressure load history. Moreover, the crack pattern observed under high pressure was less dense and featured narrower cracks compared to the 40 mm thick reference specimens under the lowest pressure. The crack widths remained below 0.1 mm. These findings emphasize the reliability of the layered retrofitting strategy, even under shock wave pressure loads.

Notably, Ultrasonic Pulse Velocity (UPV) and pull-off test results indicated the absence of delamination or detachment as a result of the shock wave tests. That implies that neither the shear stresses nor the internal stress wave reflection, arising from differing impedance between layers, induced any damage at the interlayer interface, ensuring robust bonding between the materials. This observation is crucial, signifying that shock wave application does not compromise adhesion among layers, preserving the layered solution's energy absorption capacity. This capability remains intact even when subjected to hard, localized impacts coupled with pressure waves, which are common in realistic blast scenarios. Additionally, this solution is highly resistant to localized impact effects.

The 100 mm thick slabs showed cracks only due to internal stresses resulting from the support conditions. The amplitudes of the deformations and velocities of the 100 mm thick RC and layered slabs were very similar. However, the damping ratio of the 100 mm thick RC slabs was higher, indicating a higher extent of damage. Nevertheless, the damping ratios scattered a lot, and their evaluation would have been more significant if they had been determined in a free vibration phase after the experiments. The UPV measurements supported the more serious damage of the 100 mm thick RC specimens compared to the layered ones, as proposed by the damping ratio. The internal damage of the 100 mm thick RC slabs was higher, indicating more microcracking because the UPV after the experiment was 10 % smaller than before the experiment. By contrast, the UPV decreased by less than 3 % in the case of the high-pressure experiments performed on the layered specimens.

It is worth noting that although the 100 mm thick samples exhibited no cracks after the high-pressure load, the representativeness of these results is limited when considering a potential retrofitting technique for several reasons. Firstly, a simple increase in thickness leads to a substantial rise in the global mass and stiffness of the structure, which can be disadvantageous under normal loading conditions, such as live loads and seismic actions. Most importantly, however, a simple increase in the thickness of the C35/45 structure is not suitable for retrofitting against localized impact loads that occur after the blast wave due to accelerated fragments. As a strengthening against this kind of loading, the strengthening structure consisting of ILC and SHLC[3] was found to be very expedient [15].

Considering the above, the layered solution can be deemed an effective retrofitting strategy against both blast and localized impact loading. It enhances the construction's resistance to shock wave applications indicated by small deformations, and the low level of damage experienced by the solution after the shock wave does not compromise its excellent localized impact resistance performance. The proposed novel layered solution provides comprehensive protection to the structure against all blast-induced actions that may occur during an extreme event.

6. Conclusion

The shock tube experiments carried out under two different pressure levels have proved the efficiency of the layered impact protection structure compared to the reference RC slabs. The high deformations and damage of the 40 mm thick RC slabs are contrary to the small deformations and damage of the 100 mm thick RC slabs. The layered slabs, in turn, behave equally to the 100 mm thick RC slabs, making them a very suitable choice under bending loads due to blast waves. They were neither debonded nor strongly deformed. Moreover, the layered option is also the best choice for localized impact loading and adds minimum weight to existing structures, which is beneficial for static reasons.

CRediT authorship contribution statement

Lena Leicht: Conceptualization, Methodology, Software, Validation, Formal analysis, Investigation, Data curation, Writing – original draft, Writing – review and editing, Visualization. **Matteo Colombo:** Conceptualization, Methodology, Validation, Investigation, Writing – original draft, Writing – review and editing, Project administration. **Paolo Martinelli:** Conceptualization, Methodology, Validation, Investigation, Writing – original draft, Writing – review and editing. **Cesare Signorini:** Conceptualization, Investigation, Writing – original draft, Writing – review and editing. **Viktor Mechtcherine:** Supervision, Project administration, Funding acquisition. **Marco di Prisco:** Conceptualization, Supervision, Project administration. **Silke Scheerer:** Conceptualization, Writing – review and editing, Supervision, Project administration, Funding acquisition. **Manfred Curbach:** Conceptualization, Supervision, Project administration, Funding acquisition. **Birgit Beckmann:** Conceptualization, Validation, Writing – review and editing, Supervision, Project administration.

Declaration of competing interest

The authors declare that they have no known competing financial interests or personal relationships that could have appeared to influence the work reported in this paper.

Acknowledgments

Data availability

Data will be made available on request.

References

[1] Krauthammer T. Modern protective structures. CRC Press; 2008, p. 1–511. http://dx.doi.org/10.1201/9781420015423.

[2] Bangash MYH. Data on Missiles, Impactors, Aircraft and Explosions. In: Shock, Impact and Explosion: Structural Analysis and Design. Berlin: Springer; 2009, http://dx.doi.org/10.1007/978-3-540-77068-8_2.

[3] Hering M, Bracklow F, Scheerer S, Curbach M. Reinforced Concrete Plates under Impact Load—Damage Quantification. Materials 2020;13(20). http://dx.doi.org/10.3390/ma13204554.

[4] Kühn T, Hering M, Häußler-Combe U, Curbach M. Dynamic behavior of reinforced slabs - Blast testing. In: 5th International Conference on Protective Structures. Poznan; 2018, p. 485–93.

[5] Schenker A, Anteby I, Gal E, Kivity Y, Nizri E, Sadot O, et al. Full-scale field tests of concrete slabs subjected to blast loads. Int J Impact Eng 2008;35(3):184–98. http://dx.doi.org/10.1016/j.ijimpeng.2006.12.008.

[6] Colombo M, Martinelli P, di Prisco M. Layered high-performance concrete plates interacting with granular soil under blast loads: An experimental investigation. Eur J Environ Civ Eng 2013;17(10):1002–25. http://dx.doi.org/10.1080/19648189.2013.841595.

[7] Adhikary SD, Chandra LR, Christian A, Ong KCG. SHCC-strengthened RC panels under near-field explosions. Constr Build Mater 2018;183:675–92. http://dx.doi.org/10.1016/j.conbuildmat.2018.06.199.

[8] Jahami A, Temsah Y, Khatib J, Baalbaki O, Kenai S. The behavior of CFRP strengthened RC beams subjected to blast loading. Mag Civ Eng 2021;103. http://dx.doi.org/10.34910/MCE.103.9.

[9] Hajek R, Foglar M, Fladr J. Influence of barrier material and barrier shape on blast wave mitigation. Constr Build Mater 2016;120:54–64. http://dx.doi.org/10.1016/j.conbuildmat.2016.05.078.

[10] Prikazchikova L. Decay conditions for antiplane shear of a high-contrast multi-layered semi-infinite elastic strip. Symmetry 2022;14(8):1697. http://dx.doi.org/10.3390/sym14081697.

[11] Raabe D, Sachs C, Romano P. The crustacean exoskeleton as an example of a structurally and mechanically graded biological nanocomposite material. Acta Mater 2005;53(15):4281–92. http://dx.doi.org/10.1016/j.actamat.2005.05.027.

[12] Li X. Nanoscale structural and mechanical characterization of natural nanocomposites: Seashells. JOM: J Miner Met Mater Soc 2007;59(3):71–4. http://dx.doi.org/10.1007/s11837-007-0043-2.

[13] Li X, Nardi P. Micro/nanomechanical characterization of a natural nanocomposite material - The shell of Pectinidae. Nanotechnology 2004;15(1):211–7. http://dx.doi.org/10.1088/0957-4484/15/1/038.

[14] Thielen M, Speck T, Seidel R. Viscoelasticity and compaction behaviour of the foam-like pomelo (*Citrus maxima*) peel. J Mater Sci 2013;48(9):3469–78. http://dx.doi.org/10.1007/s10853-013-7137-8.

[15] Leicht L. Characterization of Mineral-Bonded Composites as Damping Layers Against Impact Loading (Dissertation), Technische Universität Dresden; 2024, URL https://nbn-resolving.org/urn:nbn:de:bsz:14-qucosa2-903628.

[16] Koechlin P, Potapov S. Specificity of aircraft crash compared to other missile impacts. In: Proceedings of the 16th international conference on nuclear engineering ICONE, vol. 4, 2008, p. 285–91. http://dx.doi.org/10.1115/ICONE16-48946.

[17] Koechlin P, Potapov S. Classification of soft and hard impacts—Application to aircraft crash. Nucl Eng Des 2009;239:613–8. http://dx.doi.org/10.1016/j.nucengdes.2008.10.016.

[18] Colombo M, di Prisco M, Martinelli P. A New Shock Tube Facility for Tunnel Safety. Exp Mech 2011;51(7):1143–54. http://dx.doi.org/10.1007/s11340-010-9430-7.

[19] Andreotti R, Colombo M, Guardone A, Martinelli P, Riganti G, di Prisco M. Performance of a shock tube facility for impact response of structures. Int J Non-Linear Mech 2015;72:53–66. http://dx.doi.org/10.1016/j.ijnonlinmec.2015.02.010.

[20] Vismann U, editor. Wendehorst Bautechnische Zahlentafeln. 35. Springer Vieweg; 2015, http://dx.doi.org/10.1007/978-3-658-01689-0.

[21] DIN Deutsches Institut für Normung eV. Handbuch Eurocode 2: Betonbau (Band 1). DIN Deutsches Institut für Normung e.V.; 2012.

[22] Signorini C, Bracklow F, Hering M, Butler M, Leicht L, Schubert T, et al. Ballistic limit and damage assessment of hybrid fibre-reinforced cementitious thin composite plates under impact loading. J Build Eng 2023;80:108037. http://dx.doi.org/10.1016/j.jobe.2023.108037.

[23] Colombo M, Martinelli P, Arano A, Øverli JA, Hendriks MA, Kanstad T, et al. Experimental investigation on the structural response of RC slabs subjected to combined fire and blast. Structures 2021;31(June):1017–30. http://dx.doi.org/10.1016/j.istruc.2021.02.029.

[24] Cao MS, Sha GG, Gao YF, Ostachowicz W. Structural damage identification using damping: A compendium of uses and features. Smart Mater Struct 2017;26(4). http://dx.doi.org/10.1088/1361-665X/aa550a.

[25] Dieterle R, Bachmann H. Experiments and models for the damping behavior of vibrating reinforced concrete beams in the uncracked and cracked conditions. Basel: Birkhäuser; 1981, p. 69–82.

[26] Bovsunovsky AP, Surace C. Considerations regarding superharmonic vibrations of a cracked beam and the variation in damping caused by the presence of the crack. J Sound Vib 2005;288(4–5):865–86. http://dx.doi.org/10.1016/j.jsv.2005.01.038.

[27] Daneshjoo F, Gharighoran A. Experimental and theoretical dynamic system identification of damaged RC beams. Electron J Struct Eng 2008;8(8):29–39. http://dx.doi.org/10.56748/ejse.897.

[28] Kiral Z, Içten BM, Kiral BG. Effect of impact failure on the damping characteristics of beam-like composite structures. Composites B 2012;43(8):3053–60. http://dx.doi.org/10.1016/j.compositesb.2012.05.005.

[29] Beltrán R. Untersuchung von ermüdungsbedingten Veränderungen der Ultraschallgeschwindigkeit in Beton. In: BeiträGe zum 61. forschungskolloquium des deutschen ausschusses für stahlbeton. 2022, p. 71–6. http://dx.doi.org/10.25368/2022.380, URL https://nbn-resolving.org/urn:nbn:de:bsz:14-qucosa2-818382.

[30] Schickert M. DGZfP-Merkblatt B04 - Ultraschallverfahren zur zerstörungsfreien Prüfung im Bauwesen. In: Tagungsband der DGZfP Jahrestagung 2019, Friedrichshafen. 2019, URL https://www.ndt.net/article/dgzfp2019/papers/P15.pdf.

[31] Cattaneo S, Rosati G. Direct tension tests on high performance concrete specimens. In: Proceeding of the 5th international symposium on utilization of high strength/high performance concrete. 1999, p. 1063–72.